The Astronomical Journal, 149:156 (16pp), 2015 May doi:10.1088/0004-6256/149/5/156
© 2015. The American Astronomical Society. All rights reserved.

# TRACKING THE GEYSERS OF ENCELADUS INTO SATURN'S E RING

C. J. Mitchell[1], C. C. Porco[1], and J. W. Weiss[2]
[1] Cassini Imaging Central Laboratory for Operations, 4750 Walnut Street Suite 205, Boulder, CO 80301, USA
[2] Saint Martin's University, Lacey, WA 98503, USA
*Received 2014 December 11; accepted 2015 March 2; published 2015 April 14*

## ABSTRACT

We examine *Cassini* Imaging Science Subsystem images of the E ring taken over a period of almost 7 yr, from 2006 September to 2013 July, in which long, sinuous structures dubbed tendrils are present. We model these structures by numerically integrating the trajectories of particles launched from the sources of the most active geysers recently located along the four main fractures crossing the south polar terrain of the moon, and producing from these integrations synthetic images that we then compare to the real ones. We include the effects of charging and the electromagnetic forces on the particles in addition to the gravity of Saturn and Enceladus. We demonstrate that these structures are produced by the highest velocity particles erupting from the most active geysers and entering Saturn's orbit, and not perturbations of E ring particles by Enceladus. The detailed structures of the tendrils change with the orbital position of Enceladus, a finding likely to be the result of the diurnal variability in the source activity.

*Key words:* planets and satellites: rings

## 1. INTRODUCTION

During the course of the *Cassini* mission to Saturn, the Imaging Science Subsystem (ISS) took a series of low-resolution images of Enceladus and the surrounding E ring at a range of phase angles, sub-spacecraft latitudes on Enceladus, and distances. Long, narrow, arcuate, azimuthally asymmetric structures in the E ring near Enceladus, dubbed "tendrils," were first noticed in the first high-phase mosaic of the ring system taken in 2006 September when the Sun was occulted by Saturn from *Cassini*'s perspective (ciclops.org/view.php?id=2230). This occultation event allowed ISS to acquire several images of Enceladus at exceptionally high phase angles approaching 178°, a geometry that is normally impossible due to heating concerns for the suite of optical remote sensing instruments on board. At these very high phase angle, the E ring, which is composed of small particles ~1 $\mu$m in radius, becomes much brighter than normal due to forward scattering of sunlight and the tendril structures within it also became clearly visible (see Figure 2).

Early in the mission, it was suggested (Porco & Cassini Imaging Team 2006) that these structures might be related to the dozen or so jets of fine icy particles that *Cassini* had discovered in images taken in 2005 erupting from the south polar terrain (SPT) capping the moon (Porco et al. 2006), but detailed information about source locations and the directions of the jets (i.e., tilts and azimuths) were not yet in hand.

Since then, a handful of other images of the tendrils have been acquired for the express purpose of understanding their origins and relationship, if any, to the jetting activity ongoing at Enceladus south pole. The jets have been shown to be geysers, consisting of water in both vapor and solid form, the latter no doubt the result of the freezing of droplets of liquid water, deriving from a sub-ice-shell sea of liquid water. In addition, in a *Cassini* imaging survey of the SPT (Porco et al. 2014) over the course of ~7 yr, ~100 narrow geysers were found erupting from the four most prominent fractures crossing the region. Their source locations were determined to sufficient accuracy to demonstrate a spatial coincidence between several geysers on the Baghdad Sulcus, near the south pole, and small-scale (~10s of meters wide) hot spots observed by *Cassini* Visual and Infrared Mapping Spectrometer (VIMS). A measure of the relative strength of each geyser was also given in that work.

The spatially integrated plume created from the eruptions of all the jets across the SPT was observed by both VIMS (Hedman et al. 2013) and ISS (Nimmo et al. 2014) to be temporally variable; the diurnal cycling of tidal stresses across the region is likely responsible for the variation, and the phase of the plumes variability indicates other effects, perhaps resonantly forced rotational libration or a significant delay in the eruptions, are at work (Nimmo et al. 2014). Individual geysers apparently turn on and off randomly, the implication being that tidal stresses modulate the strength of the eruptions but never cause them to cease entirely (Porco et al. 2014)

In simulating the high phase narrow-angle ISS images of Enceladus plume taken during the 2006 September event, Ingersoll & Ewald (2011) found that the initial velocity distribution of the grains leaving the surface is best described by an exponential function with a characteristic velocity of 90 m $s^{-1}$. Their simulations did not take the grain charging and electromagnetic forces into account, as they were not attempting to follow particles into the E ring and their simulations were of short duration. They also did not use the actual source locations of the jets, as these were not publicly available at the time, instead using a set of 20 sources placed randomly in the area around the Tiger Stripes, south of 72° south latitude, within the SPT region surrounding the stripes.

Kempf et al. (2010) studied the vertical structure of the E ring near Enceladus by performing simulations similar to what we present here and comparing the results to measurements of the Cosmic Dust Analyzer (CDA). Their simulations did include charging of the grains and additionally followed the particles down to the surface and calculated deposition rates.

In none of the simulation work described above were precise positions and/or directions of the actual geysers used as the results of that work were not yet available. In this paper, we utilize the recently published geyser source locations, as well as their tilts and azimuths (Figure 1), and numerically integrate the equations of motion of particles launched from the most

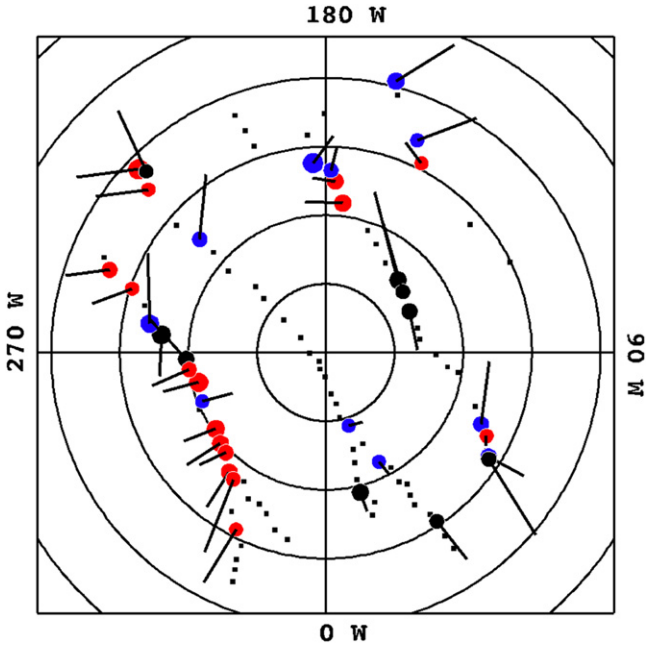


**Figure 1.** Source locations (boxes) plotted around the south pole (center) with the 36 most active jet sources marked (circles) and color coded by the behavior of the emitted grains. Red sources produce leading features, blue produce trailing, and black produce mixed. Circle size is proportional to the source activity level. Latitudes are plotted every 5°. Lines emanating from sources are the projection of the source central emission vector onto the ringplane. Saturn is down and orbital motion to the right.

active geysers in order to reproduce the tendril structures, and compare them with the actual tendril images. We include charging and electromagnetic forces in these simulations, as the particles that make up these structures are typically small ($\sim$1 $\mu$m) in radius and their trajectories cover tens of days, conditions under which electromagnetic perturbations to the orbits can become significant.

Our main goal here is to test the hypothesis that the tendrils are produced by the geysering at Enceladus's south pole by relating, if possible, tendril structures to particular geysers or geysering regions on the surface. This will help in constraining the particle size and velocity distributions for these regions. It will also help us describe the small particle environment surrounding Enceladus and thereby provide context for the interpretation of other *Cassini* data.

## 2. OBSERVATIONS

The observations used in this paper consist of ISS images taken at very high phase angle through various spectral filters over brief intervals of time, with the longest observation lasting $\sim$105 minutes. For the purposes of this paper, we initially examined only the wide-angle camera (WAC) images from all observations containing tendrils: the tendrils extend many thousands of kilometers away from Enceladus and are typically not evident in the accompanying narrow-angle cameras (NACs) due to the factor of ten difference in field of view of the cameras and the diffuse nature of the tendrils. However, due to the very high solar phase at which these images were taken, stray light can be a serious problem for the WAC images. Over the period from 2012 September to 2013 July, eight observations were attempted, but five of those were so affected by stray light that they could not be used in the analysis.

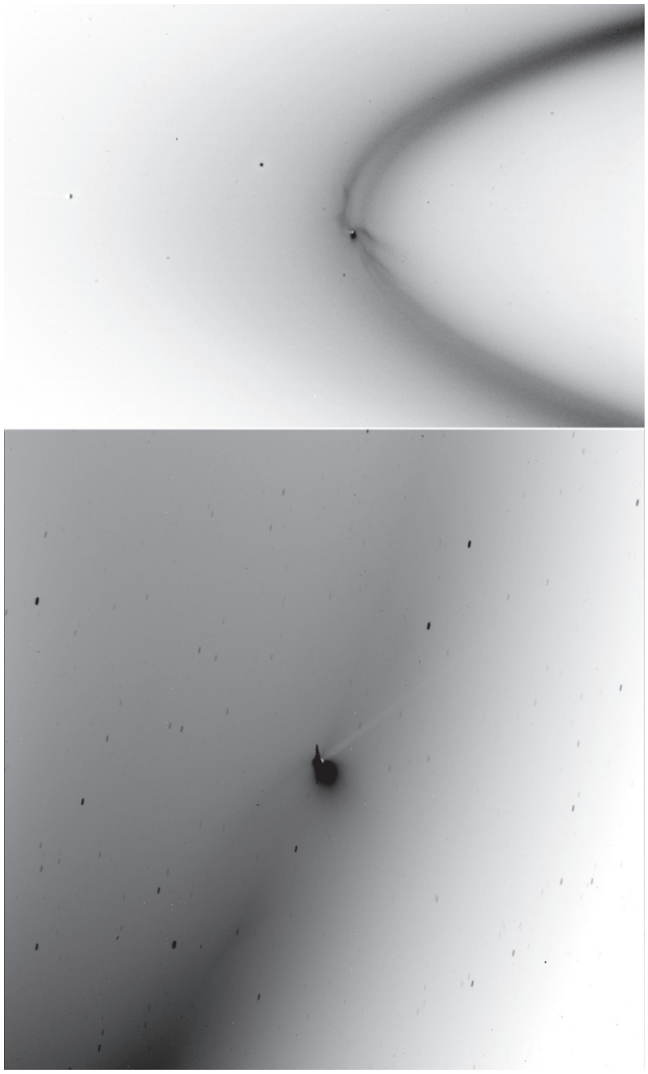

**Figure 2.** Contrast enhanced and inverted versions of the images from (top) 2006 September, and (bottom) 2013 February. Orbital motion is counter-clockwise for the top image, clockwise for the bottom. North is up in both images and Saturn is to the left in the bottom image.

The images we chose for inclusion were the least affected by stray light artifacts, and they come from four observing periods: one from the 2006 September high-phase mosaic, one taken 2013 February 25, two taken 2013 June 12, and one from the 2013 July 19, occultation of the Sun (also called The Day the Earth Smiled: www.ciclops.org/view.php?id=7699). Table 1 lists the images used in this paper, along with their geometrical characteristics and the Enceladus orbital position (or mean anomaly). Figures 2 through 4 are contrast enhanced versions of the images, all oriented so north is up.

## 3. PARTICLE DYNAMICS AND CHARGING

The equation of motion for a charged micron-sized ice grain in a planetary magnetosphere is

$$\ddot{\boldsymbol{r}} = -\nabla\Phi_G + \frac{q}{m}\left(\boldsymbol{E} + \frac{\dot{\boldsymbol{r}}}{c} \times \boldsymbol{B}\right) \quad (1)$$

where $\Phi_G$ is the gravitational potential, $\boldsymbol{B}$ the magnetic field, $\boldsymbol{E}$ the corotational electric field due to the magnetosphere–

**Table 1**
The Image Number and Date; Phase Angle, Sub-spacecraft Latitude, and Sub-spacecraft West Longitude on Enceladus; Enceladus Mean Anomaly; and Sky Plane Pixel Scale at Enceladus for the Images Analyzed in this Paper

| Image ID | Date | Phase Angle (°) | Sub-spacecraft Latitude (°) | Sub-spacecraft West Longitude (°) | Enceladus Mean Anomaly (°) | Pixel Scale (km) |
|---|---|---|---|---|---|---|
| W1537013154 | 2006 Sep 15 | 174.7 | 15.33 | 96.6 | 10 | 127.0 |
| W1740486700 | 2013 Feb 25 | 161.1 | −19.23 | 302.4 | 187 | 40.6 |
| W1749711485 | 2013 Jun 12 | 160.4 | −22.36 | 271.2 | 122 | 41.1 |
| W1749717792 | 2013 Jun 12 | 163.0 | −17.17 | 287.5 | 141 | 44.2 |
| W1752971847 | 2013 Jul 19 | 171.1 | −18.24 | 74.3 | 304 | 75.5 |

**Note.** Negative values denote southern latitudes.

ionosphere connection, $m$ the mass of the grain, $q$ the grain charge, $c$ the speed of light, and a dot represents a derivative with respect to time.

For the gravitational potential, we have:

$$\Phi_G = -\frac{GM_S}{r}\left(1 - J2_S\left(\frac{R_S}{r}\right)^2 P_2(\cos(\theta))\right) - \frac{GM_{Enc}}{||\boldsymbol{r} - \boldsymbol{r}_{Enc}||} \quad (2)$$

where $r$ is the distance from Saturn, $\theta$ is the polar angle, $GM_S = 3.793 \times 10^{22}$ cm$^3$ s$^{-2}$ is Saturn's mass times the gravitational constant ($G$), $P_n$ the $n$th order Legendre polynomial, $J2_S = 1.629 \times 10^{-2}$ is Saturn's oblateness, $R_S = 60{,}268$ km is Saturn's equatorial radius, and $GM_{Enc} = 7.210 \times 10^{15}$ cm$^3$ s$^{-2}$ is Enceladus's mass times $G$ as per Jacobson et al. (2006). Enceladus's oblateness, $J2_{Enc} = 5.4 \times 10^{-3}$ (Iess et al. 2014), is small and has been neglected to speed the simulations. (Including $J2_{Enc}$ would have the effect of slightly lowering the escape speed of the grains launched from near the south pole.)

For the magnetic field we use the latest model up to the octupole term from Burton et al. (2010). This model is completely axisymmetric, so the magnetic field is determined by taking the negative gradient of the potential function:

$$\Phi_B = \sum_{n=1}^{3}\left(\frac{R_s}{r}\right)^{n+1} g_{n0} P_n \cos(\theta) \quad (3)$$

where, in units of nT, $g_{10} = 21136$, $g_{20} = 1526$, and $g_{30} = 2219$ are the dipole, quadrupole, and octupole coefficients of the magnetic field, respectively. The corotational electric field is a function of the magnetic field and the bulk plasma flow velocity:

$$\boldsymbol{E} = -F_{corot}(\boldsymbol{\Omega} \times \boldsymbol{r}) \times \boldsymbol{B}/c \quad (4)$$

where $\Omega$ is the planetary rotation rate (approximately $1.638 \times 10^{-4}$ s$^{-1}$ for Saturn), $\boldsymbol{\Omega} \times \boldsymbol{r}$ is the corotation velocity, and $F_{corot}$ is the fraction of corotation. Since the bulk plasma flow near Enceladus has been observed to be sub-corotation (Thomsen et al. 2010), we take the flow to be 70% of corotation ($F_{corot} = 0.7$), the approximate value for the water group ions in Figure 15 of Thomsen et al. (2010) at $L = 4$, Enceladus's L shell. This has an effect on both the Lorentz force on the particles, as the electric field is 30% weaker than it would be if the plasma were corotating, and the charging of the grains, as the Mach number in the ion collection currents is reduced. For these simulations we take the magnetic field to be the unperturbed field due to Saturn only, neglecting Enceladus's effect on the field (Simon et al. 2014). We also neglect the plasma density enhancements near Enceladus, leaving both for future work.

In the above Equation of motion, we have neglected various forces on the grains that affect the very long term ($\sim 10^5$ yr for Poynting–Robertson drag) behavior of the particles but not the relatively short-term, $<10^3$ hr trajectories that we are interested in here. These include forces due to ion and neutral drag as well as the Poynting–Robertson effect. The effects of these forces are imperceptible on the short time scales that we are considering here (Goldreich & Tremaine 1982).

To find $q$, the charge on a grain as a function of time, one simply integrates the charging currents

$$\dot{q} = \sum_j I_j \quad (5)$$

where the $I_j$ represent all of the currents present in the magnetosphere (see, for example, Horányi 1996).

For our simulations, we include collection currents for two ion species (hydrogen and a water group ion we take to be singly ionized atomic oxygen), the photoelectron current due to solar UV radiation, collection currents for two populations of electrons (hot and cold), and secondary electron currents from the two electron populations. We account for the bulk plasma flow in the ion collection currents but neglect it in the electron currents as their thermal speed is much greater than the relative velocity of the grains to the plasma. The plasma parameters used for this paper are from the latest *Cassini* measurements (Sittler et al. 2005; Schippers et al. 2008; Persoon et al. 2009; Thomsen et al. 2010) and are shown in Table 2. (The value of the cold electron density has been chosen to ensure a neutral plasma.)

We take for the ice grains a density of $\rho = 1$ g cm$^{-3}$ and photoelectron coefficient of $\kappa = 0.1$, which is typical for dielectric materials such as water ice. For the secondary electrons, we take the yield to be $\delta_M = 2$ and the peak energy $E_M = 500$ eV (Horanyi et al. 1992). (Our secondary parameters differ from that of Kempf et al. 2006 due to the differences in the plasma densities and temperatures used.)

The equilibrium potential is most sensitive to the cold electron temperature, with the grain equilibrium potential becoming more negative with higher temperature. We find that for the range of cold electron temperature between 1 and 2 eV (Sittler et al. 2005; Schippers et al. 2008; Persoon et al. 2009), the equilibrium potential ranges from approximately −2 to −3 V, respectively. In situ measurements of the charge on E ring ice grains near Enceladus by CDA indicate an equilibrium

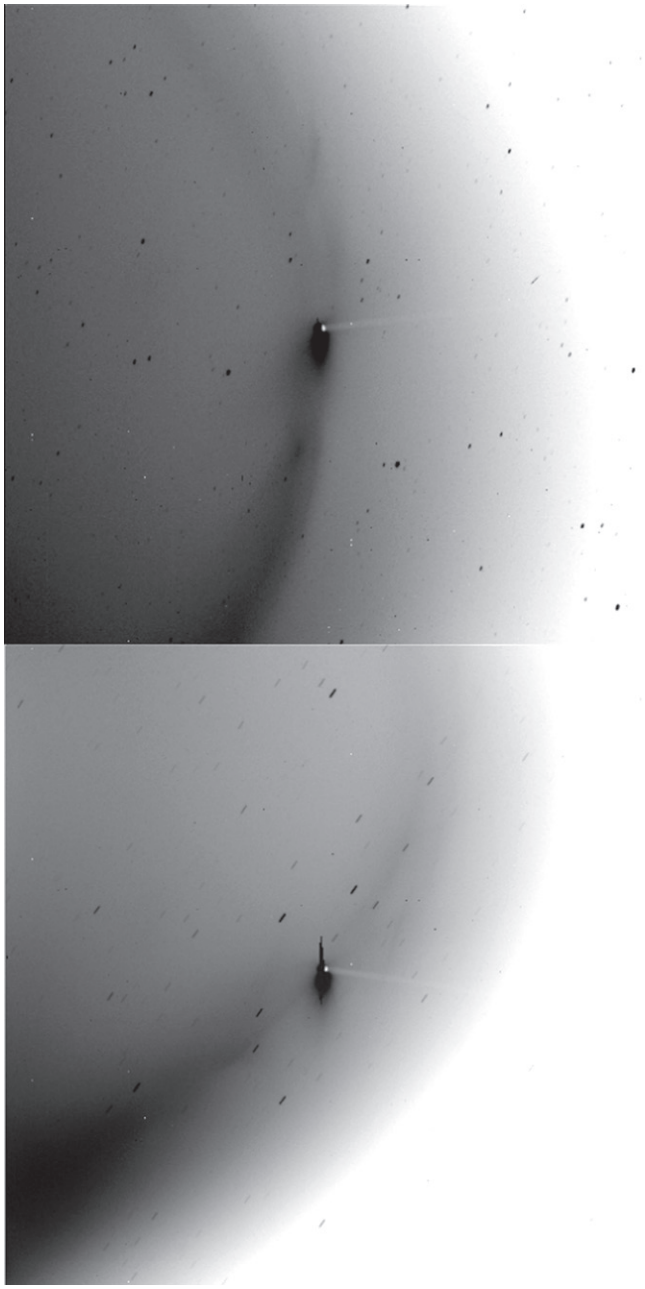

**Figure 3.** Contrast enhanced and inverted versions of the images from (top) initial 2013 June image, and (bottom) final 2013 June image. Orbital motion is clockwise and north is up in both images.

potential of −2 V (Kempf et al. 2006), we therefore use the lower, 1 eV cold electron temperature in our simulations. While the velocity distributions of both populations of electrons have been measured to be non-Maxwellian (Schippers et al. 2008), the deviation is quite small, with kappa values of approximately 20 for the cold electrons and 10 for the hot electrons, and we find that using the Kappa distributions reported produced no significant change in the charging of the grains. We also find that replacing the oxygen ions with another water group ion, such as $OH^+$ or $H_2O^+$ produced no significant change. Photoelectrons and hot electrons contribute little to the charging, the former due to the distance from the Sun and the latter due to secondary electrons canceling out the collection current.

**Table 2**
The Density and Temperature for the Plasma Constituents Used for this Paper

| Species | Density ($cm^{-3}$) | Temperature (eV) |
|---|---|---|
| $H^+$ | 5.0 | 4.0 |
| $O^+$ | 55.0 | 40.0 |
| Hot $e^-$ | 0.3 | 800. |
| Cold $e^-$ | 59.7 | 1.0 |

**Note.** The cold $e^-$ density was chosen to preserve charge neutrality.

Due to the density of the plasma, charging times are in general short, on the order of 20 minutes for a 0.1 $\mu$m grain. As the charging time for an ice grain is inversely proportional to the grain radius, the micron-sized grains reach their equilibrium charge rapidly and become fully charged well before they leave Enceladus's Hill sphere, ∼1100 km from the surface.

## 4. SIMULATIONS AND SYNTHETIC IMAGE CONSTRUCTION

For our simulations we use a publicly available fourth order Runge–Kutta integrator with an adaptive step size (Press et al. 2002). This code is both well-tested and robust enough to handle the equations of motion and charging, and has been used previously for calculating the trajectories of uncharged particles in the edge waves produced by Pan and Daphnis (Weiss et al. 2009). For this paper, we have modified the code to include charging and electromagnetic forces as described above.

As the magnetic field has been found to be axially symmetric to very high precision, there is no measurable variation in the field over a Saturnian rotation and we take it to be constant and defined by the coefficients derived by Burton et al. (2010). As Enceladus's orbital inclination and eccentricity are both small, we take these to be zero to simplify these early simulations. In future work, we will accommodate both.

We do not account for the quantized nature of the charging currents nor the random fluctuations about the mean. The random fluctuations will be on the order of a few percent: for example, a 0.25 $\mu$m grain has about 400 extra electrons at the equilibrium potential of −2 V, and so fluctuations of about 20 elementary charges are to be expected, or about 5%. The fluctuations are unlikely to be important initially, though on time scales of multiple orbits, their effect may add up to cause features to become non-coherent.

We also do not account for interparticle interactions in the simulations. These can also be important if the grain number density is large enough that the average interparticle spacing is on the order of a Debye length or less. For the plasma parameters used in our simulations, the plasma has a Debye length of 94 cm, so grain densities greater than ∼1 $m^{-3}$ would start showing these effects. For an assumed grain density of 1000 $m^{-3}$ and grain radius of 1 $\mu$m at the base of the plume, we find a $P$ value, a measure of how much grain charging affects the background plasma (Graps et al. 2008), equal to 1.4. This implies corrections to the grain charge of ∼40% (Havnes et al. 1990), with the correction decreasing with smaller density. This will have the effect of reducing the electron current and thus increasing the charging time during the initial portion of the trajectory within the dense plume. We neglect

this reduction in this paper as it is in the initial charging phase of the grains, when the charges are small, and so the Lorentz force is also small.

### 4.1. Geysers

The individual geysers were chosen for the simulations based on their measured activity (Porco et al. 2014). Out of the 101 distinct, narrow geysers identified on the tiger stripes crossing SPT of the moon, there are 98 whose tilts and activity levels have been estimated. We take the 36 most active jets to use in the simulations: together they provide ~50% of the total measured activity.

The direction of the initial velocity vector of each launched grain is determined by taking the orientation of the jet determined by Porco et al. (2014) and giving it an additional small tilt, $\Delta\Theta$, in a random azimuthal direction. The magnitude of $\Delta\Theta$ is weighted with a Gaussian, the width of which is given by the uncertainty in the jet direction reported by Porco et al. (2014); the azimuthal direction is uniformly distributed over 360 deg.

The initial speed of the grains is also randomly determined. As per the findings of Ingersoll & Ewald (2011), we take the probability distribution to have the form $e^{-v/v_0}$ where $v$ is the speed of the grain and $v_0$ is a characteristic velocity of the jets with a value of $90\,\mathrm{m\,s^{-1}}$. We chose a minimum value of $200\,\mathrm{m\,s^{-1}}$ for the velocity of the grains, slightly less than Enceladus's escape speed of $239\,\mathrm{m\,s^{-1}}$, as we are interested in grains that escape the moon.

For our initial simulations, we conducted runs with particles ranging in size from 0.125 to 2 $\mu$m, varying the particle size in steps of a factor of $2^{1/8}$. With the magnetospheric parameters used in these simulations, we found that the behavior of 2 and 1 $\mu$m grains are nearly indistinguishable from uncharged grains, while the 0.125 $\mu$m grains' motion is greatly perturbed by the Lorentz force. As such, large particles launched from the jets either lead or trail Enceladus in its orbit depending on which direction the jet pointed. Small particles, on the other hand, always eventually lead Enceladus due to electromagnetic effects, regardless of their initial launch directions, and typically form structures with very long wavelength that are not observed in the images. The transition from trailing to leading occurred around approximately 0.25 $\mu$m.

We therefore ran our simulations with particles ranging from 0.25 to 1 $\mu$m in radius, stepping by a factor of $2^{1/2}$. As the acceleration due to the Lorentz force on a grain goes as $1/r_g^2$, each step in grain size alters the size of the perturbation of the Lorentz force by a factor of 2. We ran a total of 1000 particle trajectories for each grain size for each jet source. Trajectories that impacted Enceladus were rejected and reran with new initial conditions until the particle escaped.

To produce a synthetic image from the trajectories, we use *Cassini*'s latitude and longitude on Enceladus to calculate the image plane, which is then broken up into synthetic image pixels. The trajectories of the grains are projected into this plane and the amount of time the grains spends in a pixel is taken to be proportional to that grain's contribution to the pixel's brightness. To more accurately determine the time spent in a pixel, the trajectory is interpolated between the recorded points. Thus a bright pixel in the synthetic image could be either from many particles passing through that pixel or from particles moving slowly through the pixel. As we are simply trying here to reproduce the structures and relative brightnesses of the tendril structures, and since the phase angle variation across the tendril structures in any one image is very small, we do not need to be concerned with deriving absolute brightnesses or absolute particle number densities. A more proper treatment of the brightness would require parameterizing the particle size distribution in order to calculate the appropriate particle phase function and consequently the amount of light they scatter. That is left for a future paper.

To determine how well the behavior of the individual jets can be constrained, we took the 36 jets with the greatest activity as reported in Porco et al. (2014; comprising over 50% of the total integrated jet activity) and ran the simulations five times for each jet: once with the jet ignoring the error in the jet's direction, two simulation runs with the zenith angle altered by its error, both positively and negatively, and two simulations with the azimuthal angle altered in the same way. For jets with azimuthal errors of 360°, meaning no constraint on the azimuthal direction, we took the error to be 90° so that the range of azimuthal angle was a full 180°.

For each of these 36 jets, we ran the five different simulations for three particle sizes (0.25, 0.5, and 1.0 $\mu$m) for a total of 15 simulations for each jet and qualitatively analyzed the behavior. A jet simulation was rated as being in one of three categories: either leading (with most particles moving ahead of Enceladus in its orbit), trailing, or mixed. Across the whole suite of simulations, every jet was given a score based on how consistent its behavior was; that score was the number of simulations in the most populated category. A given jet could therefore score from a minimum of 5 with all three categories equally represented, to a maximum of 15 with all the simulations behaving the same way: i.e., all leading, all trailing or all mixed.

Of these 36 most active jets, 12 scored a perfect 15: that is, the trajectories of the particles all displayed the same behavior regardless of particle size and jet direction. Ten of these jets are on Damascus Sulcus, with the other two located on Baghdad, and all launched grains onto leading trajectories. Since the Lorentz force at Enceladus's orbital radius tends to cause negatively charged grains to become more leading, varying the grain size (and thus the perturbation from the Lorentz force) did not alter the general behavior of these grains.

Of the remaining 24 jets, 14 had scores between 10 and 14, meaning that the simulations had the same behavior at least two thirds of the time, while 10 had scores less than 10, indicating that the behavior of the grains was not well defined.

### 4.2. E Ring

In addition to the grains emitted by the jet sources, the images also contain the background E ring particles. To simulate this background, we alter the initial conditions of the simulations so that the particles begin "upstream" of Enceladus (that is behind Enceladus for particles with a smaller semimajor axis and ahead of Enceladus for particles with a larger one) and run the simulation until the particles have had sufficient time to encounter the satellite and travel several more orbits to produce wave features in the density. Analysis of ISS WAC images indicates the particles near Enceladus have orbital eccentricities ranging from 0 to 0.25, and inclinations about half their eccentricities (Hedman et al. 2012). Hence, we choose an exponentially decaying distribution function for both $e$ and $i$, and for each of the simulated E rings, we calculate three sets of trajectories with mean eccentricities of 0, $2 \times 10^{-3}$, and

$2 \times 10^{-2}$, and with mean inclinations equal to half the mean eccentricity. As it turns out, particles on orbits with radial excursions *ae* much greater than the Hill radius cannot form features localized near Enceladus. We take the semimajor axis distribution of these particles to be a Gaussian centered on Enceladus with a full width of 12 Hill radii. As we are attempting only to explain the features in the immediate vicinity of Enceladus, grains with larger or smaller semimajor axes are ignored.

However we find that no azimuthal features are produced in the E ring through interaction with Enceladus when the orbital eccentricity of the particles is $\geqslant 2 \times 10^{-2}$, and so we do not include particles with larger orbital eccentricities. Our E ring simulations (discussed below) are produced only with the lowest eccentricity population.

## 5. COMPARISON WITH DATA

For each of the images listed in Table 1, we create a simulated E ring using trajectories of uncharged particles as described above and also compute simulated images for each of our 36 selected jets for each grain size, to determine whether the tendril features can be reproduced. We then compare these simulations to the real image, using these results we determine how well the 36 most active jets are able to reproduce an image, how well the E ring simulations reproduce said features, and finally attribute the features to individual jets or families of jets, that is to say, jets that launch particles in a similar direction from Enceladus.

For each image, we perform a simple linear stretch, as well as version that has been filtered by subtracting the local median of the image. At each point in the image the median value was calculated using the points falling within a $25 \times 25$ pixel window centered on the pixel. This median image was then subtracted from the actual image and the result was then stretched to bring out the detail. This procedure removes large scale variations from the image, such as the smoothly varying background E ring, but leaves structures which vary abruptly, over short length scales, such as the tendrils. Some images were then median filtered with a $5 \times 5$ window if the features are difficult to visually separate from the noise.

Before going into the specifics for individual images, a few general points can be made. The first is that the simulations of the E ring never produced a good match to any feature in any image. Figure 5 compares the results of these simulations to the 2013 July observation. As can be seen from the figure, E ring particles with 0 orbital eccentricity produce waves due to their gravitational interaction with Enceladus, but the density enhancements and rarefications have wavelengths longer than the length scales seen in the image's features, and there are often gaps in the simulations not in evidence in the iamges. Particles with more realistic—small but non-zero—orbital eccentricities do not produce features at all. The tendril structures, we thus conclude, are not produced by long-resident E ring particles perturbed by Enceladus.

Also, we find that grains as small as 0.25 $\mu$m produce features that have length scales longer than those appearing in the images and therefore we do not include them in the synthetic images presented here. This result holds true for all the images; consequently we only produce synthetic images for 0.5–1.0 $\mu$m grains emanating from the jet sources.

### 5.1. 2006 September

The first image we attempt to simulate, Figure 6, comes from the high-phase mosaic taken on 2006 September 15 during an occultation of the Sun by Saturn. This rare viewing geometry aloud the image to be taken at a phase angle of $174\overset{\circ}{.}7$ at Enceladus. The Sun is off the right side of the image and the phase angle in the E ring increases to approximately 176° on the far right side.

In this image, the sub-spacecraft latitude on Enceladus is approximately 15° N and *Cassini*'s orientation is such that the satellite's north pole is pointing upwards. Orbital motion is counterclockwise, with the leading portion of the E ring in the lower right portion of the picture. The leading hemisphere of Enceladus is nearly face-on in the image, and the leading portion of the E ring is closer to the spacecraft than the trailing portion.

The top two panels of Figure 6 shows the the median filtered version of the image and the simulation results for the 36 most active jets. The most prominent feature in this image is the tendril immediately interior to Enceladus, which we shall refer to as the "Interior Tendril." There are also features leading Enceladus ("Leading Tendrils") and trailing Enceladus ("Trailing Tendrils"). The "Trailing Tendrils" are exterior to Enceladus, but there is also material interior to Enceladus, which can be seen in the upper right of the image.

For this image, simply using the 36 most active jets produced good results, as can be seen in Figure 6. The "Interior Tendril" is clearly visible in the synthetic image to the right of Enceladus. Features can also be seen in the simulation that correspond to the "Leading Tendrils," though they appear to be more coherent (repeating over more orbits) in the simulations than the actual features in the image. This may be due to stochastic charging or interparticle forces, as explained previously.

The "Trailing Tendrils" are also apparent in the simulations, however, the trailing material interior to Enceladus is absent. This is unsurprising, as the simulations were restricted to only a few tens of orbits and to produce an interior trailing feature, the grains would have to orbit completely around Saturn in the frame of reference corotating with Enceladus, which takes considerably longer. This limited simulation time is also responsible for the simulated image density fading out far from Enceladus.

The lower left panel of Figure 6 shows the result of a simulation in which we have chosen from the 36 most active jets those which seem to reproduce the features in the image, while the lower right panel maps these jet sources around the south pole. We find that the jet sources that reproduce the "Interior Tendril" tend to be the sources along the Damascus Sulcus, which tend to launch particles in the direction opposite of Enceladus's orbital motion. There also appears to be a contribution from two jet sources on Baghdad and perhaps one on Cairo. These sources also reproduce the "Leading Tendrils" feature. The "Trailing Tendrils" feature is best reproduced by two jet sources on Cairo and one on Baghdad.

Figure 7 shows the results of scanning along the E ring both the actual image and the synthetic image at three radii from Saturn. As the simulations lacked an E ring, a quadratic background has been added to the scans of the synthetic image. This background was taken by selecting the points on the extreme ends of the scan as well as some points in the middle

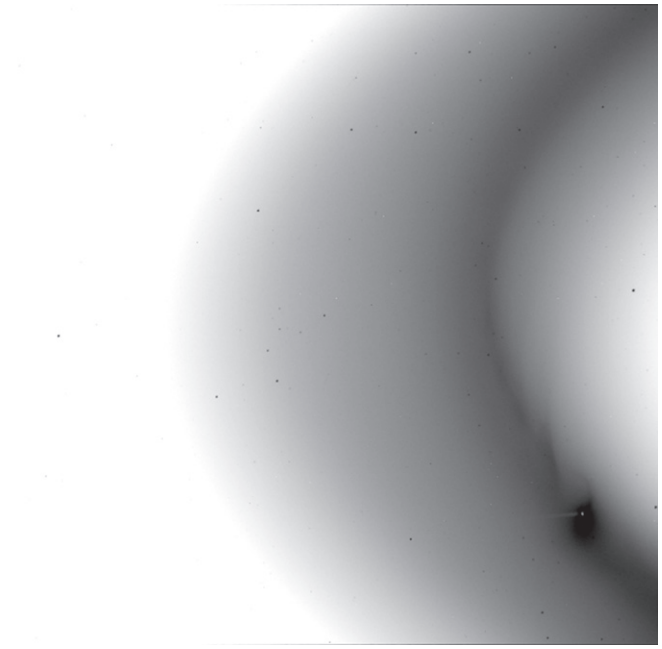

**Figure 4.** Contrast enhanced and inverted version of the 2013 July image. Orbital motion is clockwise and north is up.

of the scan, which were apparently free of Tendril material, and fitting a quadratic to them.

The image scans show local brightness enhancements due to the Tendril features, with several local maxima in the scans for both the leading and trailing portions. Generally speaking, particles will produce a density enhancement every half orbit as they near one of the radial turning points. Successive enhancements move farther away from Enceladus with time. These features also appear in the scans of the synthetic image, but there are differences.

First, the peaks in the scans are shifted longitudinally from the real peaks. This is likely due to Enceladus's own orbital eccentricity, which we do not account for in these simulations. For a body with purely gravitational dynamics such as Enceladus, the azimuthal motion in the mean motion reference frame has an amplitude of $2ae$, where $a$ is the semimajor axis and $e$ the eccentricity. For Enceladus's orbit, $ae$ is approximately 1000 km, and $2ae$ corresponds to a longitude variation of $0\overset{\circ}{.}5$, which can account for most of the shift.

Also, as mentioned previously, the features in the synthetic image persist farther away from Enceladus than the real features, possibly due to stochastic charging or interparticle interactions, as mentioned previously.

### 5.2. 2013 February

The median filtered version of the 2013 February image can be seen in Figure 8. It has a phase angle of $161\overset{\circ}{.}1$ at Enceladus and a spacial resolution higher than the previous one, 40.6 km pixel$^{-1}$. The Sun is off the lower left corner of the image, as can be seen by the shadow of the satellite on the E ring, which goes to the upper right. Phase angle ranges from $163\overset{\circ}{.}5$ on the lower left to $158\overset{\circ}{.}7$ on the upper right. Orbital motion is clockwise; we are looking from the south instead of the north (as in the previous image).

The feature we referred to as the "Interior Tendril" is again visible in this image, as are the "Leading Tendrils" which are

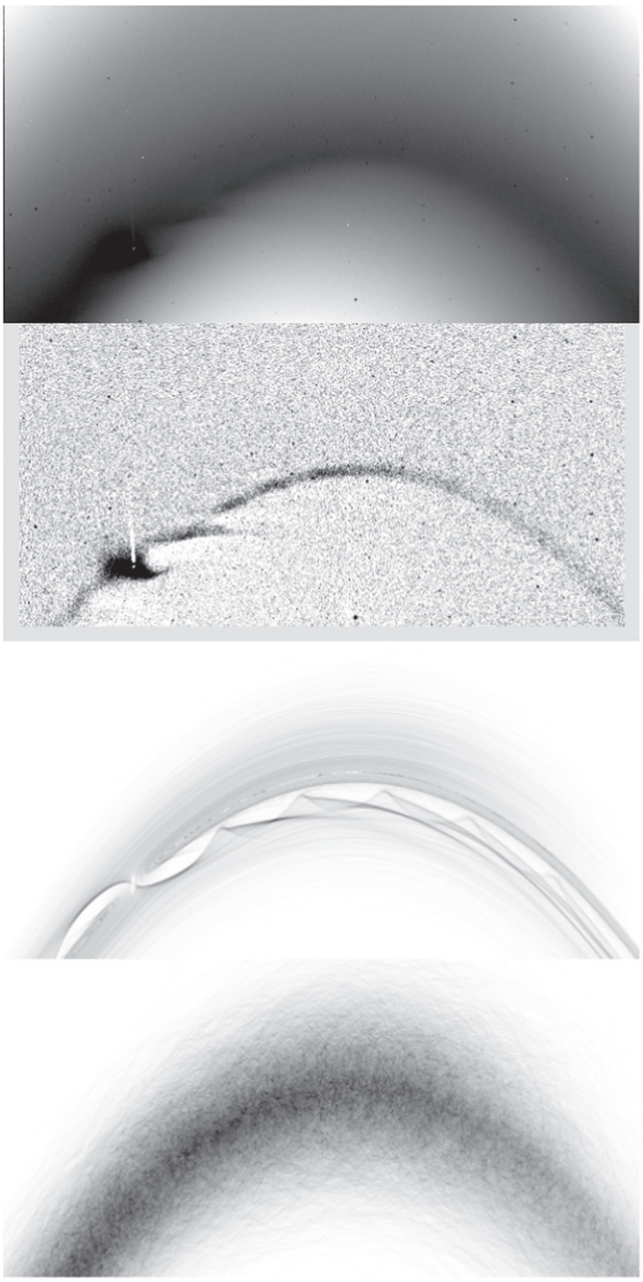

**Figure 5.** (Top) Contrast enhanced and inverted image from the 2013 July, observation showing the features near Enceladus. (Upper Middle) Median filtered version to bring out the local variations in brightness. (Lower Middle) The synthetic image produced from the simulation of E ring particles with zero orbital eccentricity. (Bottom) The synthetic image produced from the simulation of E ring particles with small $(2 \times 10^{-2})$ orbital eccentricity. Orbital motion is clockwise and all panels have been rotated so north is to the right.

below and to the left of Enceladus. There also appears to be a long linear and narrow ring extending in both leading and trailing directions and located at Enceladus's semimajor axis, with limited radial variation and width. We shall refer to this feature as the "Core." This feature is only sometimes present in the images and is difficult to reproduce in the simulations. This may indicate that the feature is either transient, only appearing in part of Enceladus's orbit, or that it is visible only in certain

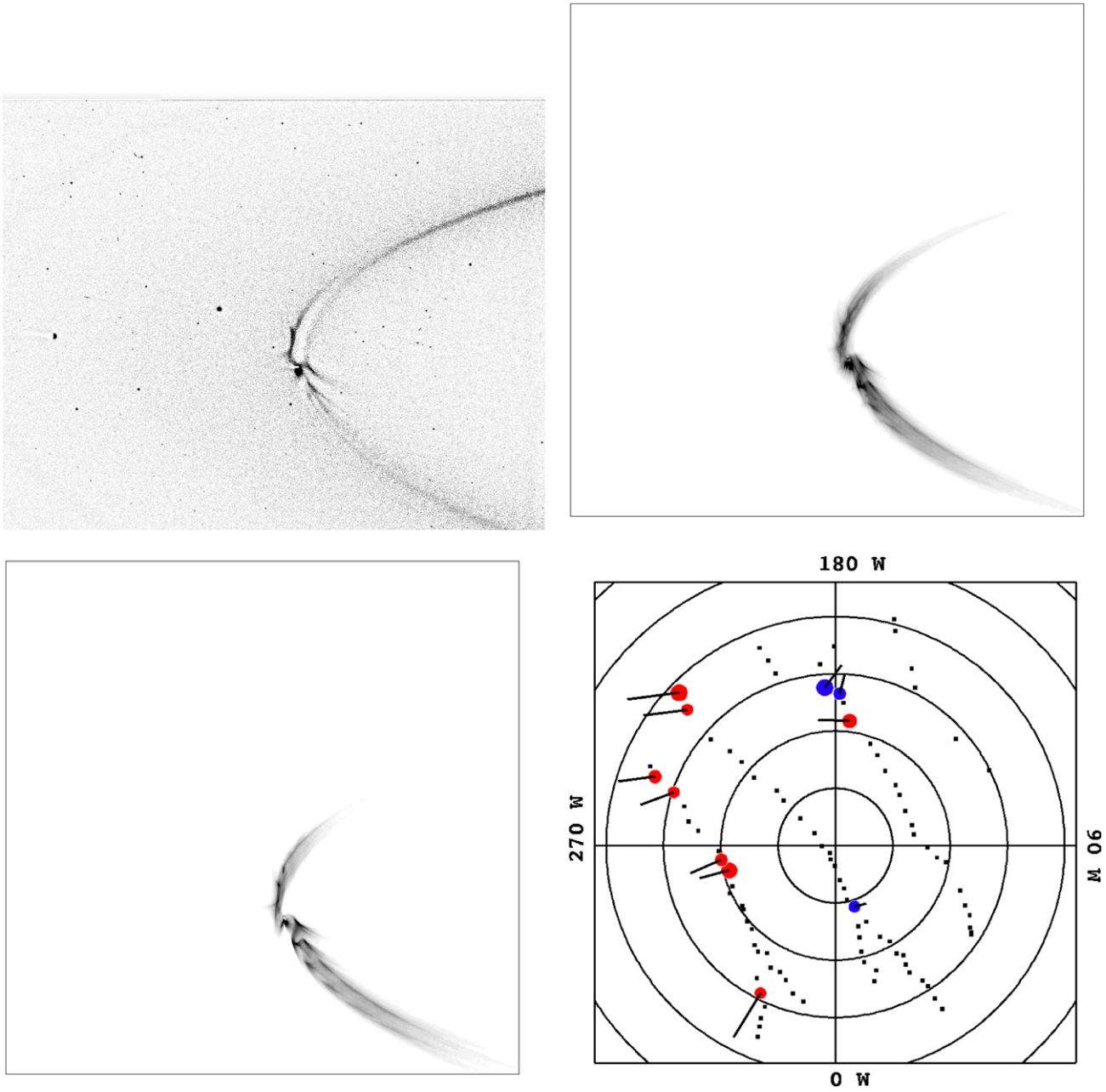


**Figure 6.** (Top Left) Median filtered version of the 2006 September observation showing the features near Enceladus. (Top Right) Synthetic image using the most active 36 jets. (Bottom Left) Synthetic image using the jets that best reproduce the image features. (Bottom Right) Map of the south pole with the chosen jets marked as in Figure 1. The synthetic images were produced using grains sizes of 0.50, 0.71, and 1.00 $\mu$m. Orbital motion is counterclockwise and north is up in the image and simulations.

geometries, where perhaps a sheet of material is visible when seen edge on but not otherwise.

For the 2013 February image, we find that simply running the 36 most active jets do reproduce some of the features in the image, with the exception of the "Core." (See Figure 8.) The "Interior Tendril," to the left of Enceladus, shows up prominently in the simulation; however, the tendril in the image is brighter closer to Enceladus, whereas in the simulation the brightness peaks downstream. This could be a manifestation of time variability in the jet sources, which is known to be present (Hedman et al. 2013; Porco et al. 2014; Nimmo et al. 2014). The "Leading Tendrils" also appear in the simulation, with a bright region overlapping the "Core" to the lower left. The lower most density enhancement in the simulations does not appear in the image, much like simulation features far from Enceladus in the previous image.

Attempting to refine our selection of sources to those that best reproduced the image features resulted in the sources and simulations presented in the bottom two panels of Figure 8. Again, sources on Damascus dominate the "Interior Tendril" and "Leading Tendrils," with some contribution from Baghdad and Cairo. Very few jets produced anything like the "Core" feature, and those that did would often produce it at an incorrect radius. We did find one jet source on Cairo that produced a similar feature, but it also produced features not seen in the actual image. This could be due to the modulation of the sources over Enceladus's orbit: i.e., not all sources will

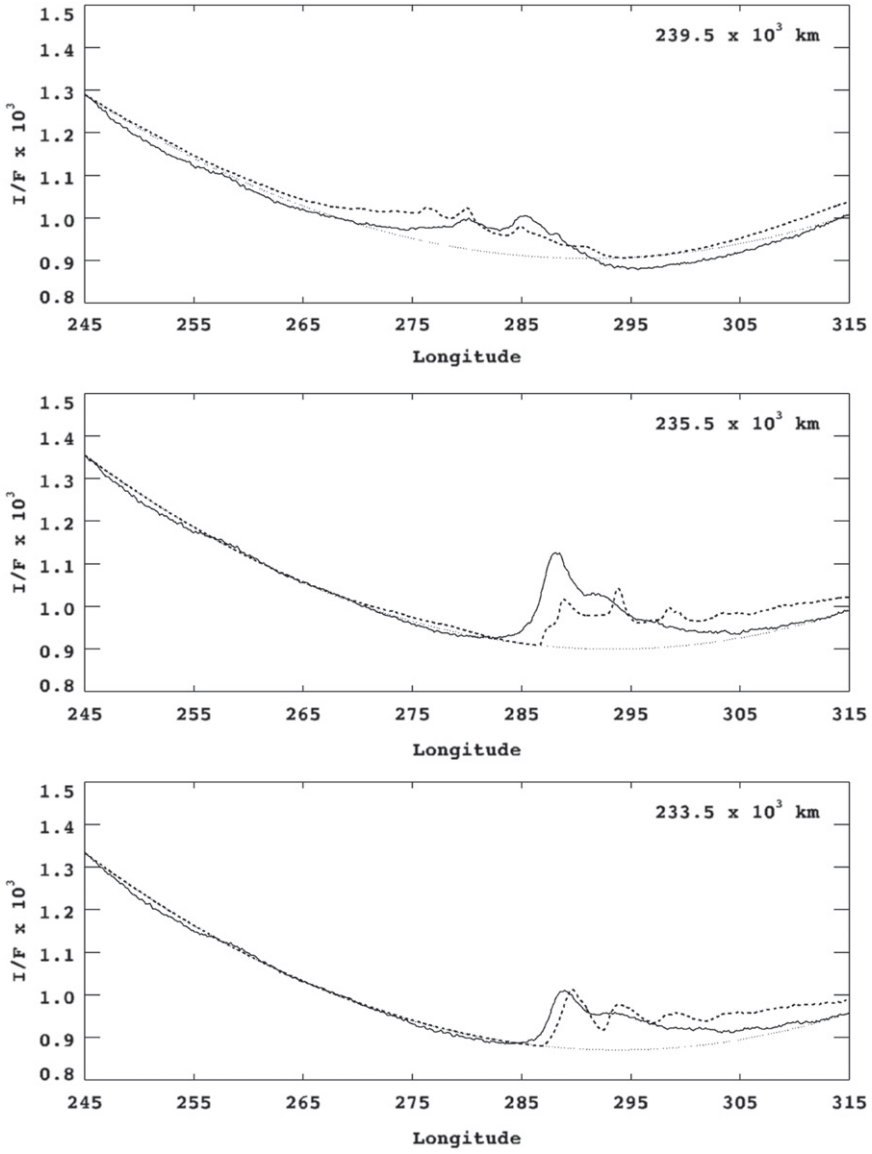


**Figure 7.** Scans of I/F vs. longitude at constant radius from Saturn in the actual image (solid) and synthetic image (dashed) at three separate radii. The dotted line is a quadratic background derived from the image and added to the synthetic image scans to make them appear on the same plot. The top plot at 239.5 $\times$ $10^3$ km is exterior to Enceladus while the lower two plots at 235.5 and 233.5 $\times$ $10^3$ km are interior. Enceladus is located at a longitude of 287.°9.

be launching particles into the E ring at the same time with the same vigor.

Figure 9 again shows the scans of the actual image and the synthetic image, plus quadratic background. As with the September image, we again have density enhancements that are slightly shifted between the actual image and the synthetic image. This turns out to also be true of the following images and we will refrain from plotting more scans.

### 5.3. 2013 June

The 2013 June observation consisted of a series of images taken over a period of about 105 minutes. Here we use the initial and final image from this observation to see whether we can produce consistent results from the first to the last. That is to say, do the jets which properly reproduce the features in the first image also reproduce those in the last?

This first image, Figure 10, is a 22 second exposure taken at 160.°4 phase at Enceladus in the CLR filter. The sub-spacecraft latitude is 22.°4 south. *Cassini* is oriented so that south is down in the image. Orbital motion is clockwise, with the upper, trailing part of the E ring closer than the lower leading portion. The Sun is off the left side of the image, with the phase in the image ranging from 162° on the left to 158° on the right.

The second image, Figure 11, is a 56 s exposure CLR taken 105 minutes after the first. The orientation is similar, with south down and clockwise orbital motion. The phase ranges from 161° to 165° in the upper left portion of the image, with the phase at Enceladus 163.°0. The sub-spacecraft latitude has changed to 17.°2 south.

In the first image, we see various features of both the "Leading Tendrils" and "Trailing Tendrils." The "Interior Tendril" is present, but it is not as bright as seen previously, another indication of temporal variability. The second image,

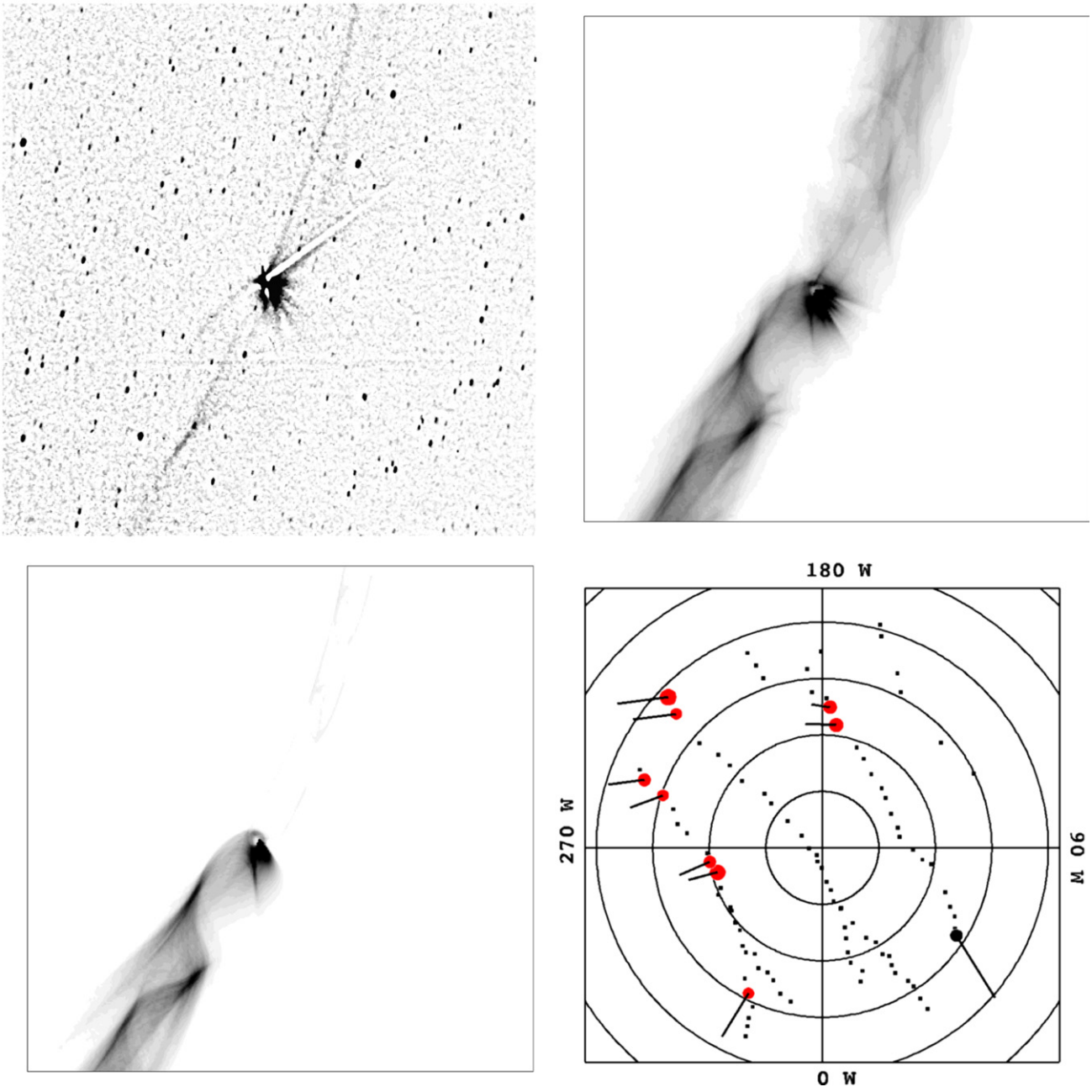


**Figure 8.** (Top Left) Median filtered version of the 2013 February observation showing the features near Enceladus. (Top Right) Synthetic image using the most active 36 jets. (Bottom Left) Synthetic image using the jets that best reproduce the image features. (Bottom Right) Map of the south pole with the chosen jets marked as in Figure 1. The synthetic images were produced using grains sizes of 0.50, 0.71, and 1.00 $\mu$m. Orbital motion is clockwise (Saturn is to the left) and north is up in the image and simulations.

on the other hand, appears to have the "Core" feature in it again. This feature was not obvious in the first image, taken 105 minutes earlier. In processing these images, the first image was subjected to a larger stretch due to its fainter features, caused by the shorter exposure time and lower phase angle. The range in I/F for Figure 10 is 50% larger than it is in Figure 11.

We first take the first image and check to see if the 36 most active jets reproduce its features, with the result shown in the upper right panel of Figure 10. The simulations do a reasonably good job of reproducing the "Trailing Tendrils" and some portions of the "Leading Tendrils," but the "Interior Tendril" is much more prominent in the simulations than in the image. (The E ring simulations, not shown, once again put features in the wrong places at the wrong angles.)

Figure 10 also shows the jet sources and simulations that best reproduce the features in the image. As there is no prominent "Interior Tendril" in the image, the best jet sources are not concentrated on Damascus in this particular case. In fact, they are composed of a mixture of leading, trailing, and mixed jets located on all four sulci. This is a departure from the previous images and is likely the effect of time variability in the sources.

In Figure 11, the results from the most active jets are compared to the actual image. The "Leading Tendrils" and

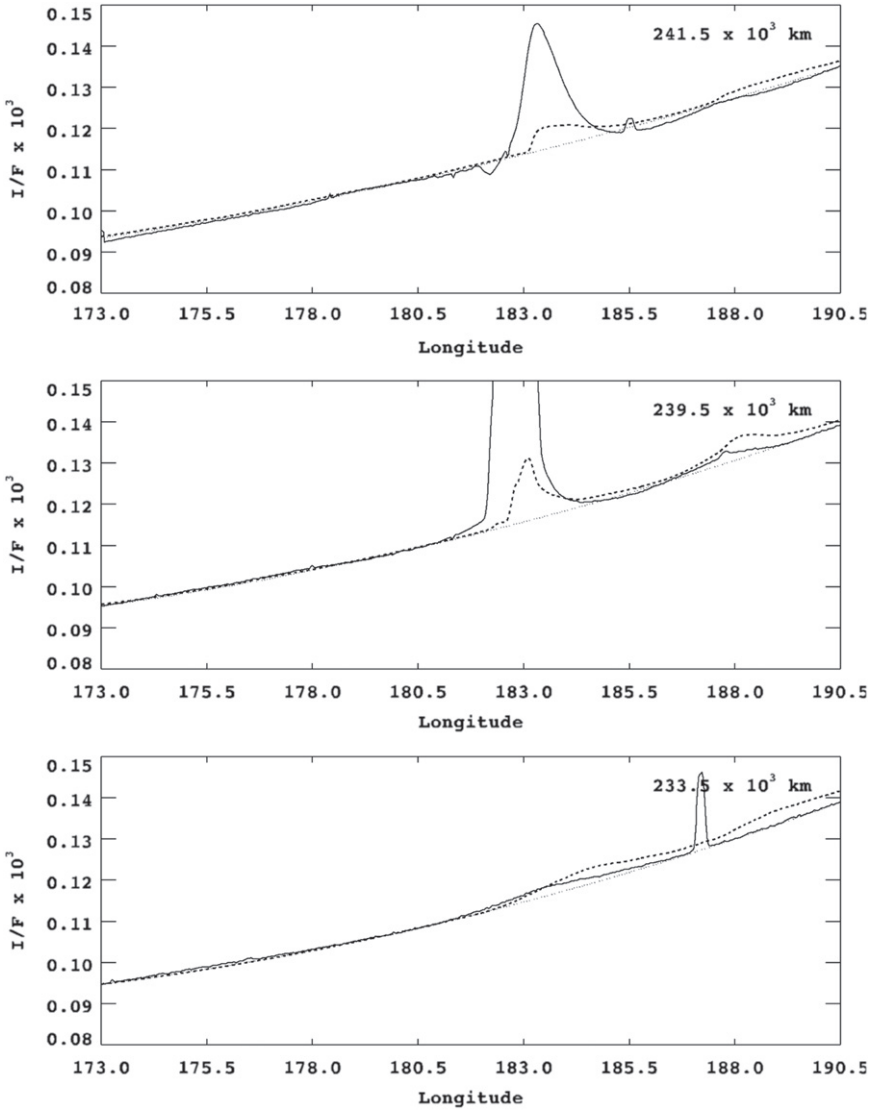


**Figure 9.** Scans of I/F vs. longitude at constant radius from Saturn in the actual image (solid) and synthetic image (dashed) at three separate radii. The dotted line is a quadratic background derived from the image and added to the synthetic image scans to make them appear on the same plot. The top two plots at 241.5 and 239.5 $\times$ $10^3$ km are exterior to Enceladus while the bottom plot at 233.5 $\times$ $10^3$ km is interior. Enceladus is located at a longitude of 182.°6.

"Interior Tendril" produced in the simulations do not appear in the actual image, while the "Core" feature appears in the actual image, but is not obvious in the simulations. However, one feature in the "Trailing Tendrils" portion of the image deoes seem to match the nearly vertical structure to the right of Enceladus. Overall, the 36 most active jets do not do a good job of reproducing this image.

We next attempt to recreate the features using the same jet sources that were chosen for Figure 10. Figure 11 also show these jet sources and the resulting synthetic image from the simulations in the bottom two panels. The "Trailing Tendrils" are reproduced reasonably well, with the near vertical feature showing up in the synthetic image. There also appears to be a possible "Core" in the trailing part of the synthetic image, though it has density fluctuations along it not present in the actual image. The leading portion of the "Core" does not appear to align with the features in the synthetic image.

In an attmept to better reproduce the "Core" feature, we now pick jets based on the behavior of their emitted particles. Figure 12 shows the results. Again we find that Damascus is not producing the features in this image and the jet sources that do appear to are located on the other sulci. We are able to find jet sources that enhance the density at the appropriate locations for the "Core," but at the same time, those sources produce features that are not in the image. (In this case, exterior to the "Core" in the "Trailing Tendrils" region.) This may again indicate time variability, if the jets were more active during the time when the "Core" was created than the other features.

We can therefore say that using the jets which reproduce one image well can do a reasonable job of reproducing an image taken a short time later, though not without some modification. Additionally, the "Core" feature is particularly difficult to reproduce, and can differ radically between images separated by 105 minutes. And, perhaps most importantly, there appears to be substantial difference in the jet sources that reproduce the tendrils well, with the features in the first two images we examined being produced primarily by sources on Damascus, while those of these two images appear to have very little contribution from it and instead appear to come from sources on the other sulci.

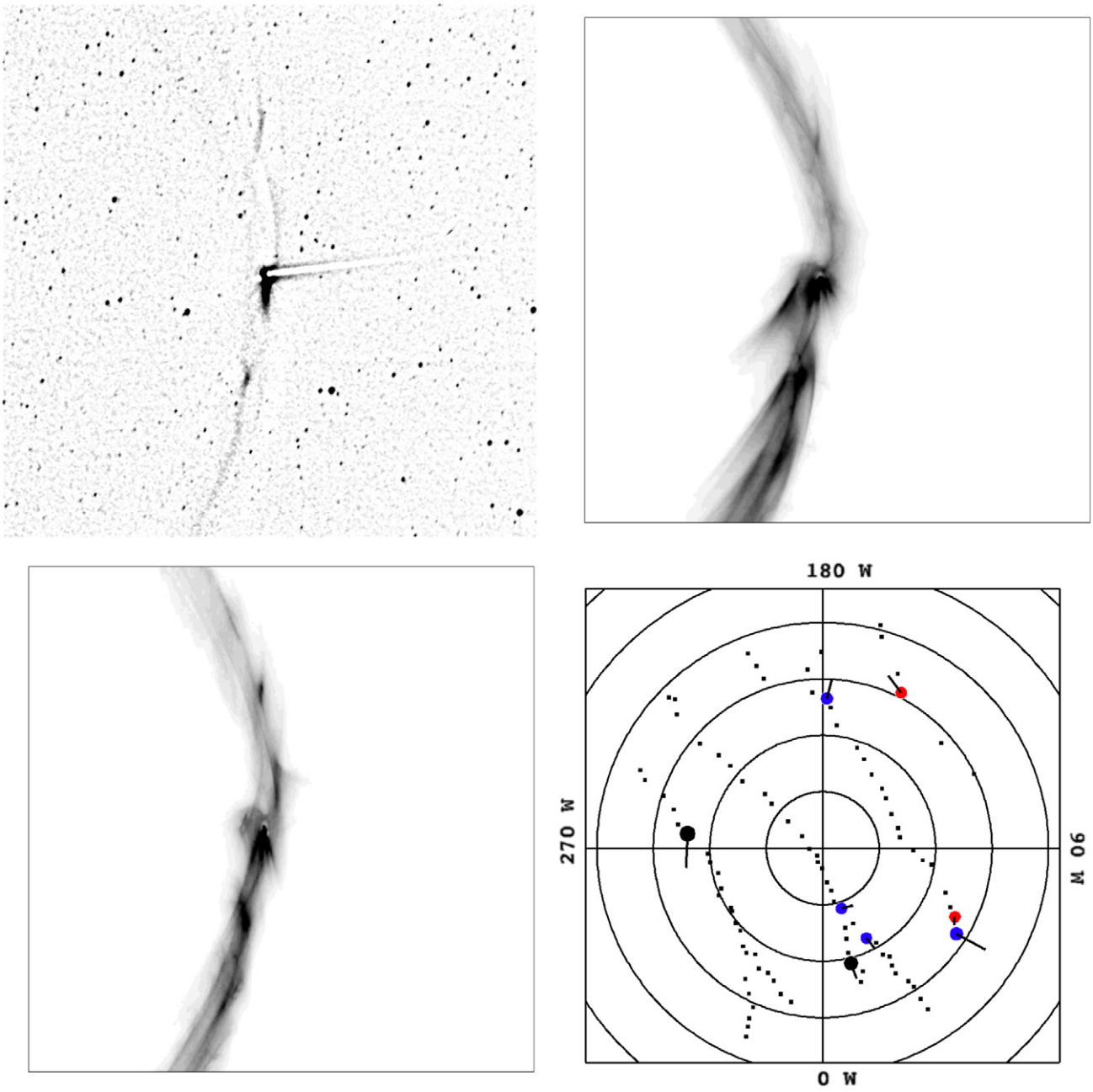


**Figure 10.** (Top Left) Median filtered version of the first image of the 2013 June observation showing the features near Enceladus. (Top Right) Synthetic image using the most active 36 jets. (Bottom Left) Synthetic image using the jets that best reproduce the image features. (Bottom Right) Map of the south pole with the chosen jets marked as in Figure 1. The synthetic images were produced using grains sizes of 0.50, 0.71, and 1.00 $\mu$m. Orbital motion is clockwise and north is up in the image and simulations.

As with the previous images, scans taken of the actual images and the synthetic images agree well, with only slight differences ($\sim 1^\circ$) in the location of the features.

### 5.4. 2013 July

The final image we consider was also taken during an occultation of the Sun, similar to the 2006 September image, although the spacecraft was considerably closer to Saturn at the time and therefore the resolution was higher.

This image was taken using the RED filter, unlike all the previous images which were all taken in CLR, however we expect there to be little difference in the image as the RED filter has an effective wavelength very close to that of the CLR filters (649 nm, vs 651 nm for CLR). The phase at Enceladus is 171.°1 in the image and the resolution is 75.5 km pixel$^{-1}$. The Sun is off the right of the image.

The most prominent features in this image are the "Leading Tendrils" and the "Interior Tendril," the latter now clearly seen to be just the first portion of the "Leading Tendrils." "Trailing Tendrils" do not appear in this image. (A search for these features in other images during the same observation period revealed none.) There does not appear to be a "Core" feature in this image.

Figure 13 shows the standard four panels. For this image, using the 36 most active jets does a very good job of reproducing the "Leading Tendrils" and the "Interior Tendril."

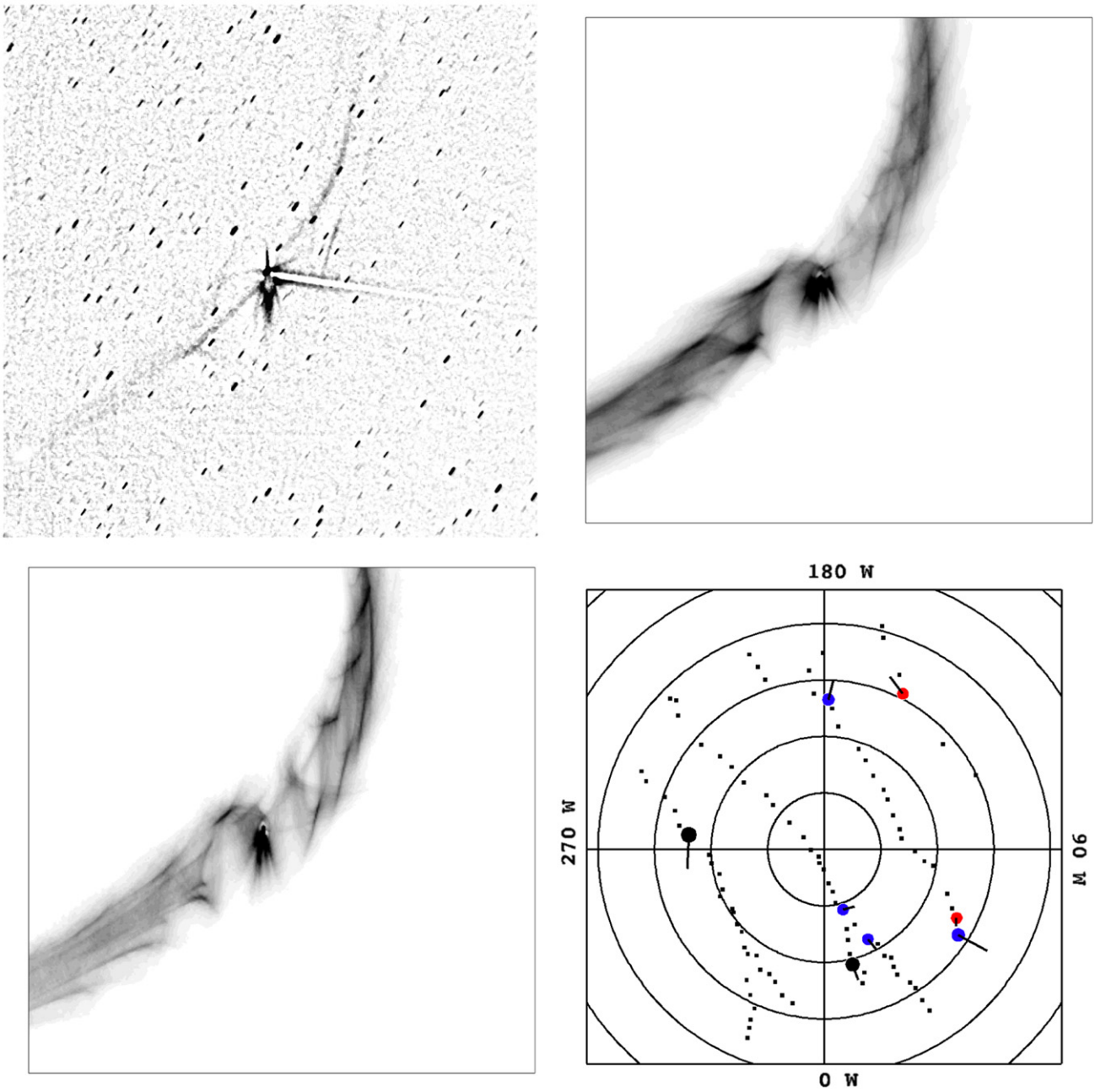


**Figure 11.** (Top Left) Median filtered version of the second image of the 2013 June observation showing the features near Enceladus. (Top Right) Synthetic image using the most active 36 jets. (Bottom Left) Synthetic image using the jets that best reproduce the previous image's features. (Bottom Right) Map of the south pole with the chosen jets marked as in Figure 1. The synthetic images were produced using grains sizes of 0.50, 0.71, and 1.00 $\mu$m. Orbital motion is clockwise and north is up in the image and simulations.

Choosing the best jet sources improves the agreement between the actual image and the simulations as can be seen in the upper right and lower left panels of Figure 13. As the image basically contains only "Interior Tendril" and "Leading Tendrils" features, all of the selected jet sources are those that produce leading particles and again the major source is Damascus, with a small contribution from Baghdad and Cairo.

## 6. DISCUSSION AND FUTURE WORK

Our examination of five wide-angle, low-resolution, high-phase ISS images taken of the E ring in the vicinity of Enceladus on four dates spanning 7 yr, and the modeling of the narrow, arcuate "tendril" features found there, shows that most of these features are indeed produced by the jets emanating from the four main fractures crossing the moons south polar region.

The two images at the highest phase and lowest resolution are reproduced well using all 36 of the most active jets. Three of the images studied in this work show "Leading Tendrils" that can be reproduced primarily by jet sources located on Damascus Sulcus, while another two, which were a mere 105 minutes apart, do not. Additionally, difficulties in reproducing the "Core" feature present in some of the images may be due to temporal variability of the jet sources. Alternatively, as the

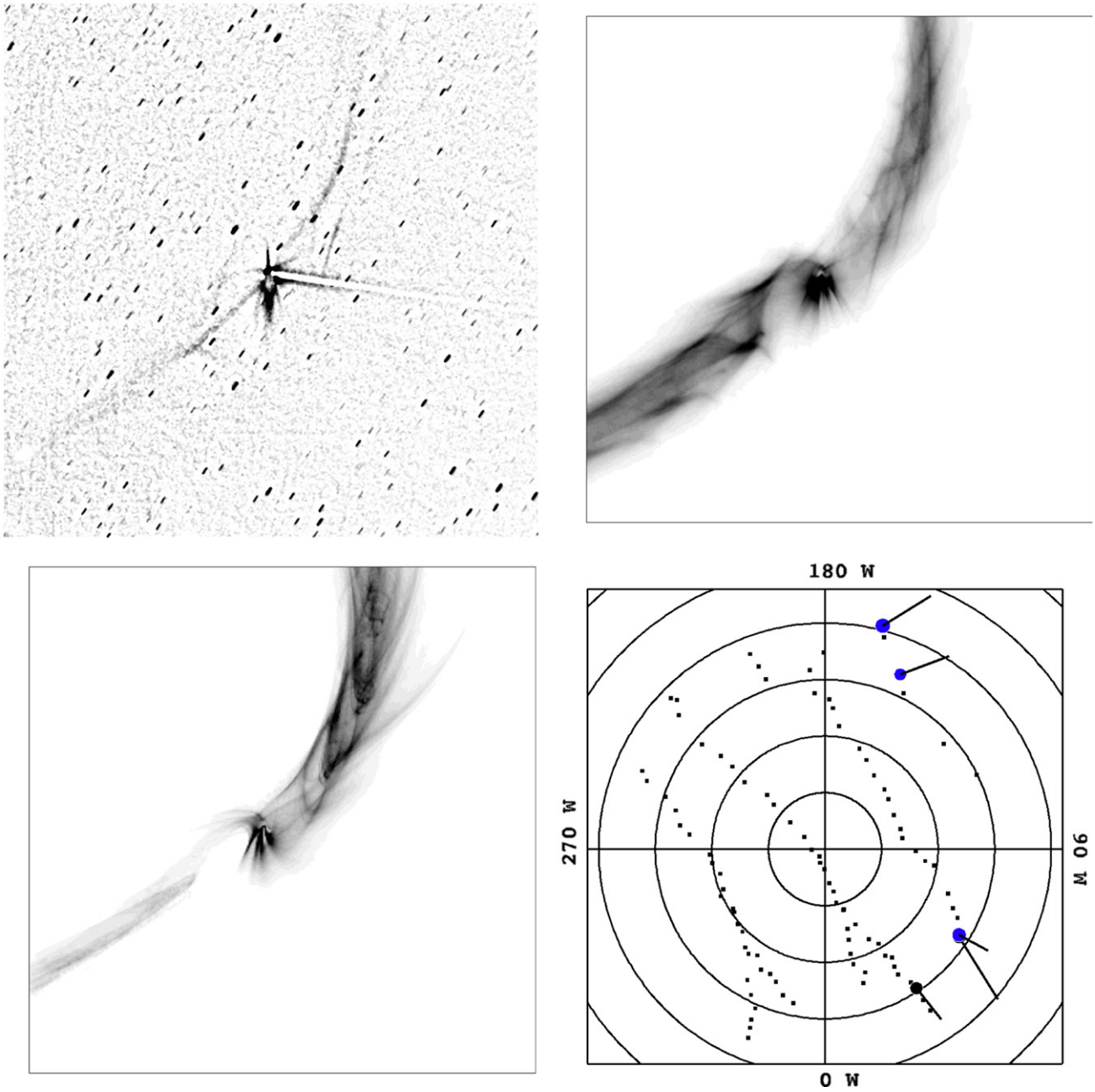


**Figure 12.** (Top Left) Median filtered version of the second image of the 2013 June observation showing the features near Enceladus. (Top Right) Synthetic image using the most active 36 jets. (Bottom Left) Synthetic image using the jets that best reproduce the "Core" feature. (Bottom Right) Map of the south pole with the chosen jets marked as in Figure 1. The synthetic images were produced using grains sizes of 0.50, 0.71, and 1.00 $\mu$m. Orbital motion is clockwise and north is up in the image and simulations.

feature appears on both sides of Enceladus, it may be due to particles that have completed an entire orbit around Saturn in the frame corotating with Enceladus. If so, we would not expect it to appear in our short-duration simulations.

In general, the "Leading Tendrils" features are produced by the sources on Damascus, with small contributions from Baghdad and Cairo, while the "Trailing Tendrils" are produced primarily by sources on Cairo and Baghdad, with some contribution from Alexandria. The "Core" feature is more difficult to interpret, due to its transient nature, but if it is not due to grains orbiting completely around Saturn, then it would be produced by jet sources on the sulci other than Damascus. Additionally, when taking longitudinal scans of the actual and synthetic images and comparing them, features often have a slight ($\sim 1^\circ$) shift in longitude. This is consistent with the displacement expected due to the orbital eccentricity of Enceladus, which we have ignored here.

The details present in the images are inconsistent with them being formed from zero eccentricity E ring particles. And E ring particles with very low orbital eccentricities ($e < 10^{-2}$) produce features that are inconsistent with the images: Waves are excited in the ring, creating density enhancements, but the wavelength in the simulations exceeds that observed in the respective images. E ring particles of higher, non-zero

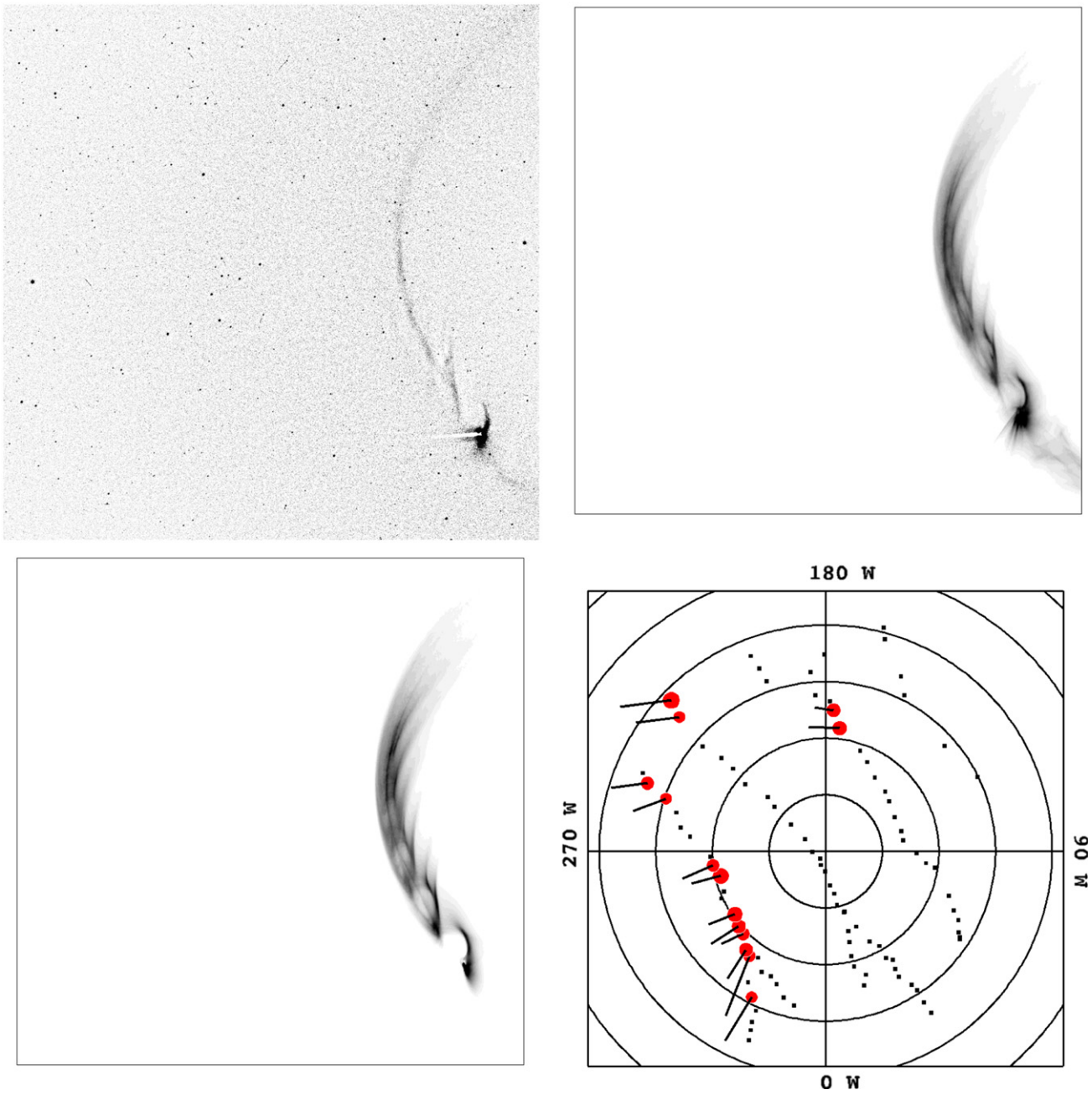


**Figure 13.** (Top Left) Median filtered version of the image from the 2013 July observation showing the features near Enceladus. (Top Right) Synthetic image using the most active 36 jets. (Bottom Left) Synthetic image using the jets that best reproduce the image features. (Bottom Right) Map of the south pole with the chosen jets marked as in Figure 1. The synthetic images were produced using grains sizes of 0.50, 0.71, and 1.00 $\mu$m. Orbital motion is clockwise and north is up in the image and simulations.

eccentricities matching those inferred from analyses of E ring images (Hedman et al. 2012) do not produce features at all.

We also find that the smallest particles considered, with radii of 0.25 $\mu$m, produce features that have length scales larger than those in the images. The tendril features apparently consist of particles 0.5 microns and larger. This is consistent with previous studies of the E ring (Hedman et al. 2009; Kempf et al. 2010).

Another interesting difference between our simulations and the images is that the "Interior Tendril" nearest to Enceladus is often brighter near the satellite in our simulations than in the images. This could be another manifestation of time variability in the sources. The diurnal variability in the brightness of the plume, as observed by Cassini, and the inferred cyclical variability in the strength of individual geysers in accord with the variation in normal stresses at the geysers' vents, would be expected to show up in the Tendrils as periodic brightness enhancements that propagate away from Enceladus and repeat at intervals equal to an orbital period along the Tendril.

Future work will include the introduction of time-variable sources as the activity of the jets is known to vary in strength as a function of Enceladus' mean anomaly owing to the cycling of tidal stresses, plus some additional effects, across the surface (Nimmo et al. 2014). Additionally, we intend to add the eccentricity and inclination of Enceladus's orbit into the simulations, and extend their duration to determine

whether the "Core" feature is due to grains completely encircling Saturn in Enceladus's mean motion frame. We shall also incorporate Enceladus's influence on the local magnetic field and plasma conditions. Finally, we will include a proper treatment of light scattering in order to derive particle number densities in the tendrils, leading the way to an additional constraint on particle escape rates from Enceladus as well as an accurate description of the particle environment in the vicinity of the moon.

The research in this paper was primarily supported by NASA CDAP and the *Cassini* mission. The authors thank Daiana DiNino for her assistance in the use of image projection software used in this paper, and Mihaly Horanyi for a conscientious review. We would also like to acknowledge the work of the CICLOPS operations staff in designing and sequencing the images used in this work.

## REFERENCES

Burton, M. E., Dougherty, M. K., & Russell, C. T. 2010, GeoRL, 37, 24105
Goldreich, P., & Tremaine, S. 1982, ARA&A, 20, 249
Graps, A. L., Jones, G. H., Juhász, A., Horányi, M., & Havnes, O. 2008, SSRv, 137, 435
Havnes, O., Aanesen, T. K., & Melandso, F. 1990, JGR, 95, 6581
Hedman, M. M., Burns, J. A., Hamilton, D. P., & Showalter, M. R. 2012, Icar, 217, 322
Hedman, M. M., Gosmeyer, C. M., Nicholson, P. D., et al. 2013, Natur, 500, 182
Hedman, M. M., Nicholson, P. D., Showalter, M. R., et al. 2009, ApJ, 693, 1749
Horányi, M. 1996, ARA&A, 34, 383
Horanyi, M., Burns, J. A., & Hamilton, D. P. 1992, Icar, 97, 248
Iess, L., Stevenson, D. J., Parisi, M., et al. 2014, Sci, 344, 78
Ingersoll, A. P., & Ewald, S. P. 2011, Icar, 216, 492
Jacobson, R. A., Antreasian, P. G., Bordi, J. J., et al. 2006, AJ, 132, 2520
Kempf, S., Beckmann, U., & Schmidt, J. 2010, Icar, 206, 446
Kempf, S., Beckmann, U., Srama, R., Horanyi, M., Auer, S., & Grün, E. 2006, P&SS, 54, 999
Nimmo, F., Porco, C., & Mitchell, C. 2014, AJ, 148, 46
Persoon, A. M., Gurnett, D. A., Santolik, O., et al. 2009, JGRA, 114, 4211
Porco, C., DiNino, D., & Nimmo, F. 2014, AJ, 148, 45
Porco, C., & Cassini Imaging Team 2006, The Geysers of Enceladus: An Overview of Cassini Results, AGU Fall Meeting Abstracts, P22B-01
Porco, C. C., Helfenstein, P., Thomas, P. C., et al. 2006, Sci, 311, 1393
Press, W., Teukolsky, S., Vetterling, W., & Flannery, B. 2002, Numerical Recipes in C++: the Art of Scientific Computing (Cambridge: Cambridge Univ. Press)
Schippers, P., Blanc, M., André, N., et al. 2008, JGRA, 113, 7208
Simon, S., Saur, J., Treeck, S. C., Kriegel, H., & Dougherty, M. K. 2014, GeoRL, 41, 3359
Sittler, E. C., Thomsen, M., Chornay, D., et al. 2005, GeoRL, 32, 14
Thomsen, M. F., Reisenfeld, D. B., Delapp, D. M., et al. 2010, JGRA, 115, 10220
Weiss, J. W., Porco, C. C., & Tiscareno, M. S. 2009, AJ, 138, 272